THE ASTROPHYSICAL JOURNAL, 561:282–298, 2001 November 1
© 2001. The American Astronomical Society. All rights reserved. Printed in U.S.A.

DUST CHARACTERISTICS OF MASSIVE STAR-FORMING SITES IN THE MID-INFRARED

KATHLEEN E. KRAEMER[1,2]
Air Force Research Laboratory, Space Vehicles Directorate, 29 Randolph Road, Hanscom AFB, MA 01731; kathleen.kraemer@hanscom.af.mil
JAMES M. JACKSON,[1] LYNNE K. DEUTSCH, AND MARC KASSIS[1]
Department of Astronomy, Boston University, Boston, MA 02215; jackson@bu.edu, deutschl@bu.edu, mkassis@bu.edu
JOSEPH L. HORA[1] AND G. G. FAZIO
Harvard-Smithsonian Center for Astrophysics, 60 Garden Street, MS-78, Cambridge, MA 02138; jhora@cfa.harvard.edu, gfazio@cfa.harvard.edu
WILLIAM F. HOFFMANN
University of Arizona, Steward Observatory, Tucson, AZ 85721; whoffmann@as.arizona.edu
AND
ADITYA DAYAL
IPAC/JPL, Caltech MS 100-22, 770 S. Wilson, Pasadena, CA 91125; adayal@ipac.caltech.edu
Received 2001 February 23; accepted 2001 July 9

ABSTRACT

Four massive star-forming regions were imaged in the mid-infrared with the MIRAC3 instrument: W51 IRS 2, Mon R2, DR 21, and S140. We obtained high spatial resolution ($\sim 1''$) images at several wavelengths from 7.8 to 13.2 μm with the circular variable filter, as well as narrow-band continuum images at 12.5 and 20.6 μm toward each region. In each massive star-forming region, one or more sources show deep silicate absorption. For at least two of the massive star-forming regions, W51 IRS 2 and Mon R2, the absorbing material is highly localized and may be circumstellar material in disks or shells. The silicate absorption occurs at least as often around massive young stars as around young stars of lower mass (which are more often observed). The estimated optical depths of the silicate features are consistent with those predicted by radiative transfer models toward ultracompact H II regions, but substantially higher than observed toward T Tauri stars and other low-mass young stellar objects. There is no consistent correspondence between silicate absorption and either the dust color temperature or the 12.5 μm opacity. In W51 IRS 2, the two previously known mid-infrared sources have been resolved into at least six subsources. Infrared counterparts are newly reported for two radio-continuum sources in S140. Also, new mid-infrared sources have been detected in both W51 IRS 2 and S140. We suggest that the infrared source in the southwest of DR 21 may not be self-luminous, but may instead be heated by the three nearby radio continuum sources. The gas density in the ring at Mon R2 supports the blister scenario for the IRS 1 H II region.

Subject headings: H II regions — infrared: ISM — ISM: individual (W51 IRS 2, Monoceros R2, DR 21, S140) — ISM: lines and bands — stars: formation

1. INTRODUCTION

When massive stars form, they have profound effects on the parental molecular clouds in which they remain most, if not all, of their lives. From within, they control the chemistry, distribution, physical conditions, and kinematics of the surrounding gas and dust. While the hardest ultraviolet (UV) photons form the H II region, softer UV radiation penetrates the surrounding molecular gas to create the photodissociation region (PDR). PDRs play a vital role in the energy balance of the interstellar medium (ISM) in that their far-infrared radiation from fine-structure lines dominates the cooling of the ISM (e.g., Tielens & Hollenbach 1985; Stacey et al. 1993). The heating and structure of PDRs, on the other hand, is dominated by dust. Far-UV radiation from massive stars is absorbed by dust grains, which eject photoelectrons. The photoelectrons collide with surrounding gas particles, thus heating the ISM. Models of PDRs (e.g., Tielens & Hollenbach 1985; Sternberg & Dalgarno 1989; Draine & Bertoldi 1996) suggest that their spatial extent is determined by the optical depth of the dust, which limits the penetration of the UV radiation into the cloud. As dust is fundamental to the structure and energetics of PDRs, in order to understand them fully, it is essential to measure their dust properties.

To that end, we are examining the dust characteristics of massive star-forming regions in the mid-infrared (mid-IR), which is particularly suited to the study of dust in PDRs. First, mid-IR emission arises from the small grains heated by the far-UV radiation of massive young stars. Second, the mid-IR does not suffer from extinction effects that hamper optical observations. Third, significantly higher spatial resolution can be achieved in the mid-IR than in the far-IR traditionally used to trace PDRs. We have chosen to initiate our investigation by studying the dust properties in four massive star-forming regions: W51 IRS 2, Mon R2, DR 21, and S140. The combination of MIRAC2/3's imaging capability and its high spectral resolution (1.8%) circular variable filter (CVF) allows the determination of not only the dust characteristics at bright IR compact sources, but also

[1] Visiting Astronomer at the Infrared Telescope Facility, which is operated by the University of Hawaii under contract from the National Aeronautics and Space Administration

[2] Institute for Astrophysical Research, Boston University, Boston, MA 02215

the spatial distribution of spectral features and hence dust properties over larger scales. Data from previous work on NGC 6334I (Kraemer et al. 1999a) and W49 (Smith et al. 2000) supplement the current data set. The observations and data reduction are described in § 2; the results are presented in § 3; the silicate absorption is discussed in § 4; and our findings are summarized in § 5.

2. OBSERVATIONS AND DATA REDUCTION

Four massive star-forming regions were imaged with the MIRAC2 and 3 systems (Hoffmann et al. 1998) at the Infrared Telescope Facility (IRTF). MIRAC2/3 is a mid-infrared array camera built for ground-based astronomy at Steward Observatory, University of Arizona and Harvard-Smithsonian Center for Astrophysics. It is an upgrade of the original MIRAC system (Hoffmann et al. 1994) that utilizes a Rockwell HF-16 128 × 128 arsenic-doped silicon blocked-impurity-band hybrid array operating in a liquid helium-cooled cryostat at 5 K. The telescope was operated in chop-nod mode with a chop frequency of 2 Hz, so the source was in the beam 25% of the time. Infrared standard stars were used to calibrate the fluxes and to calibrate the plate scale (0″.33 pixel^{-1}). The bandwidths of the 12.5 and 20.6 μm filters are 10% and 7%, respectively, and that of the circular variable filter (CVF) used for the other wavelengths is 1.8%. Table 1 summarizes the observational parameters; Table 2 summarizes the fluxes assumed for the standard stars at each wavelength. Multiple images with relative offsets of a few arcseconds were taken of each source. The images were cross-correlated to the nearest 0.25 pixel and co-added to produce the final maps. The extinction coefficients used were 0.45 mag per air mass at 20.6 μm and 0.2 mag per air mass at all other wavelengths, as suggested in the IRTF Photometry Manual (Tokunaga 1986), since there was insufficient standard star data to calculate these values.

Dust color temperature (12.5/20.6 μm) maps were produced from the ratio of the flux maps, where the dust emissivity is assumed to be proportional to λ^{-1}. Dust opacity maps at 12.5 μm were also produced by using the 12.5 μm flux maps with the color temperature maps and solving the standard radiative transfer equation. To increase the signal-to-noise, the flux maps were convolved to 2″ resolution (except W51, which had sufficiently high signal that only the 12.5 μm map was convolved, to 1″.7, the resolution of the

TABLE 1

OBSERVATIONAL PARAMETERS

Source	Wavelength (μm)	Integration Time (s)	FWHM (arcsec)	NEFD (mJy)	CVF/NB[a]	Observation Date	Standard Star
W51 IRS 2.....	7.75	150	0.82	48	CVF	1999 Sep 18	γ Aql
	8.2	150	0.87	18	CVF	1999 Sep 18	γ Aql
	8.99	150	0.88	20	CVF	1999 Sep 18	γ Aql
	10.3	150	0.89	19	CVF	1999 Sep 18	γ Aql
	10.52	150	0.88	19	CVF	1999 Sep 18	γ Aql
	11.2	150	1.04	12	CVF	1999 Sep 17	γ Aql
	12.8	150	1.07†	29	CVF	1999 Sep 18	γ Aql
	13.2	150	1.11†	46	CVF	1999 Sep 18	γ Aql
	12.5	300	1.14	13	NB	1999 Sep 16	γ Aql
	20.6	150	1.73†	72	NB	1999 Sep 18	γ Aql
Mon R2.....	8.2	150	0.78	28	CVF	1999 Sep 19	α Tau
	8.99	50	0.79	42	CVF	1999 Sep 20	α Tau
	10.3	100	0.86†	33	CVF	1999 Sep 19	α Tau
	11.2	150	0.97	32	CVF	1999 Sep 18	α Tau
	12.8	150	1.07†	47	CVF	1999 Sep 19	α Tau
	13.2	50	1.11†	174	CVF	1999 Sep 19	α Tau
	12.5	135	1.05†	28	NB	1999 Sep 18	α Tau
	20.6	160	1.73†	158	NB	1999 Sep 18	α Tau
DR 21	8.2	200	0.83	32	CVF	1999 Sep 19	γ Aql
	8.99	200	0.86	34	CVF	1999 Sep 19	β Peg
	10.52	200	0.93	21	CVF	1999 Sep 19	β Peg
	11.2	180	0.97	31	CVF	1999 Sep 19	γ Aql
	12.8	200	1.07†	42	CVF	1999 Sep 19	γ Aql
	13.2	200	1.11†	45	CVF	1999 Sep 19	γ Aql
	12.5	200	1.05†	23	NB	1999 Sep 18	γ Aql
	20.6	100	1.73†	126	NB	1999 Sep 19	γ Aql
S140	9.7	100	1.10	65	CVF	1997 Sep 14	μ Cep
	10.52	100	1.05	18	CVF	1997 Sep 14	μ Cep
	11.3	100	1.08	21	CVF	1997 Sep 14	μ Cep
	12.3	100	1.11	23	CVF	1997 Sep 14	μ Cep
	12.8	100	1.14	24	CVF	1997 Sep 14	μ Cep
	13.2	100	1.17	45	CVF	1997 Sep 14	μ Cep
	12.5	560	1.05†	23	NB	1997 Sep 14	μ Cep
	20.6	110	1.73†	137	NB	1997 Sep 14	μ Cep

NOTE—Integration times are on-source integration times. FWHM is the full- width half-maximum of a Gaussian fitted to the standard stars reduced in an identical manner to the scientific data. Those marked with an † indicate the observations were diffraction limited and the values quoted are $1.22\lambda/D$. NEFDs are 1σ point source sensitivities.

[a] Circular-variable (CVF) or narrowband (NB) filter.

TABLE 2

STANDARD STAR FLUXES

λ (μm)	Standard Star			
	α Tau	γ Aql	β Peg	μ Cep[a]
7.75	946[b]	119	...	...
8.2	867	109	...	...
8.99	741	93	450	...
10.3	603	75	372	...
10.52.....	...	73	359	1885
11.2	527	66	...	...
11.3	...	...	...	1617
12.3	...	...	...	1110
12.8	411	51	...	975
13.2	383	49	...	930
12.5	431	53	257	1033
20.6	158	20	...	793

NOTE—Adopted fluxes are a combination of Cohen et al. (1995), M. S. Hanner (1994, private communication), and Gezari et al. (1993). If more than one reference cites a flux at a given wavelength, they are averaged. If a given wavelength does not have a measured flux, it is estimated by linear interpolation of the fluxes at nearby wavelengths.

[a] Because μ Cep is variable, the adopted fluxes are from measurements with the *ISO*-SWS instrument. For verification, the S140 MIRAC fluxes were compared with measurements of S140 with *ISO*-SWS, with excellent agreement between the ground-based and satellite-based observations (Kraemer et al. 1999b), except at 12.5 μm (see text).

[b] Fluxes in Janskys.

20.6 μm image). A flux cutoff of 0.25 mJy pixel^{-1} was applied to the convolved maps prior to the calculations of the color temperature and opacity maps. Fluxes, dust color temperatures, and 12.5 μm dust opacities are reported in Table 3. Color temperatures and opacities are the average value within the given aperture. Apertures in which the flux and so on were measured were chosen to enclose the maximum flux from a particular source without overlapping with the aperture used for an adjacent source (Kraemer et al. 1999a).

Point-source sensitivities (noise equivalent flux density or NEFD) for each co-added field were calculated following the procedure described by Kraemer et al. (1999a) and are reported in Table 1. For the convolved images used to make the temperature and opacity maps, the standard deviation per pixel was 0.1 mJy, so the 0.25 mJy cutoff corresponds to 2.5 σ. Reasonable agreement was found between the fluxes given in the literature (e.g., Wynn-Williams et al. 1974; Hackwell, Grasdalen, & Gehrz 1982; Genzel et al. 1982) and in those reported here, with the exception of the 12.5 μm narrowband observations of S140. The fluxes of S140 IRS 1 and 3 at 12.5 μm were 10% lower than expected from the CVF fluxes at 12.3 and 12.8 μm, and from the *ISO*-SWS spectrum, which matches the CVF measurements extremely well (Kraemer et al. 1999b). The fluxes of S140 IRS 2 and VLA 4 were 50% and 70% lower than expected from the CVF fluxes. Because of this uncertainty in the calibration of the 12.5 μm data, fluxes, color temperatures, and opacities are not given for S140. Adjusting the 12.5 μm data by 10% (from the brighter sources IRS 1 and IRS 3) does not affect the distribution of the color temperature or opacity, so those results are included in § 3.4. Not including the S140 12.5 μm data, the absolute fluxes are estimated to be accurate to at least 10%, with the relative fluxes within a map significantly better.

Except for W51, absolute coordinates for the (0, 0) position in each map are taken from the literature. Mon R2 is centered on IRS 2 (α, δ) = ($06^h07^m45^s.67$, $-06°22'52''.6$), $\pm 1''$ (J2000) (Hackwell et al. 1982). The (0, 0) position in DR 21 is [RGG89] D at (α, δ) = ($20^h38^m1^s.26$, $42°19'53''.4$), $\pm 0''.4$ (J2000) (Roelfsema et al. 1989). The (0, 0) position in S140 is IRS 1 at (α, δ) = ($22^h19^m18^s.21$, $63°18'46''.9$), $\pm 0''.5$ (J2000) (Evans et al. 1989).

Because of the extremely deep silicate absorption feature associated with source KJD 3 in W51 IRS 2 (see § 4), determination of the absolute coordinates in W51 IRS 2 is more complicated than for the other massive star-forming regions. Because of this absorption feature, source KJD 5 is the brightest around 9–11 μm, and again at 20 μm, whereas KJD 3 dominates at the other mid-IR wavelengths. To determine the absolute coordinates of the compact sources,

TABLE 3

OBSERVATIONAL AND DERIVED RESULTS

Source		$F_{12.5}$ (Jy)	$F_{20.6}$ (Jy)	Aperture[a] (arcsec)	$\overline{T}_{12.5/20.6}$ (K)	$\overline{\tau}_{12.5\,\mu m}$ ($\times 10^{-3}$)	M_d (hot) ($\times 10^{-3}$ $M_\odot$)	n_g[b] (cm^{-3})
W51 IRS 2.....	KJD 1	29.4	62.9	1.67	159	36.7	15.4	5.4(6)
	KJD 2	26.9	55.6	1.67	164	28.3	11.3	3.9(6)
	KJD 3	23.6	35.0	1.17	172	29.6	7.1	7.2(6)
	KJD 4	6.4	18.0	0.83	145	67.9	6.7	1.9(7)
	KJD 5	16.2	39.5	1.17	154	54.5	10.7	1.1(7)
	KJD 7	1.3	5.5	1.67	130	16.3	3.4	1.2(6)
Total:		588	1522	20.0	149	8.8	500	1.0(5)
Mon R2.....	IRS 1	24.9	115.5	6.00	127	16.3	1.3	4.8(6)
	IRS 2	65.2	75.0	6.00	192	2.6	0.2	5.8(5)
	IRS 5	8.7	49.0	6.00	118	11.6	0.9	3.4(6)
	ring[c]	12.8	123.6	4.50	106	99.3	4.0	3.5(7)
DR 21	N	21.2	60.1	8.33	144	2.1	1.7	2.5(5)
	S	23.3	138.1	12.00	120	7.9	9.1	4.5(5)

[a] Photometric apertures chosen to enclose the maximum flux without overlapping an adjacent source/aperture. Because of the close spacing and extended nature of the sources, this method probably underestimates the total flux from a given subsource, particularly for W51. Color temperatures and 12.5 μm opacities are the average value within the given aperture.

[b] $a(b) = a \times 10^b$.

[c] "Ring" position used is 20.6 μm flux peak at ($-7''.6$, $-15''.8$)

the 8.2 μm data were convolved to 2″ and compared with the 8 μm map of Genzel et al. (1982). The convolved emission peak is assumed to correspond to the 8 μm position at $(\alpha, \delta) = (19^h23^m40^s.18, 14°31'6''.1)$, $\pm 1''$ (J2000) (Genzel et al. 1982). Since the convolved peak coincides with the unconvolved peak, KJD 3, the positions of the remaining sources are estimated relative to source KJD 3. Genzel et al. (1982) find the 8 and 20 μm peaks separated by approximately an arcsecond, which is consistent with the separation of KJD 3 and KJD 5. Table 4 summarizes the relative positions of the mid-IR sources in W51 IRS 2, as well as the other star-forming regions.

3. RESULTS

3.1. *W51 IRS 2*

W51 IRS 2 is part of one of the most luminous and active regions of massive star formation in the Galaxy. Also known as W51 North, it is associated with radio continuum emission (W51d, d1, and d2: e.g., Mezger & Henderson 1967; Wood & Churchwell 1989; Gaum, Johnston, & Wilson 1993), OH (Gaume & Mutel 1987), H_2O (e.g., Johnston, Sloanaker, & Bologna 1973), methanol (Slysh et al. 1999), and NH_3 (Mauersberger et al. 1987; Zhang & Ho 1995) masers, and numerous tracers of dense molecular gas. Proper motion studies of H_2O masers place IRS 2 at a distance of 8.3 kpc (Schneps et al. 1981), although as many authors adopt a distance of 7.5 kpc to match that of W51 IRS 1, we do so also for calculations. Zhang, Ho, & Ohashi (1998) recently found a compact core of 2 mm dust continuum emission and dense molecular gas near the H_2O maser but distinct from the radio continuum sources. Hackwell et al. (1982) first determined that the mid-IR emission consists of two blended sources, IRS 2 E and IRS 2 W. The fainter mid-IR source W is associated with the bright radio source W51d, whereas the brighter mid-IR source E is associated with the weaker radio emission from W51d1 (Gaume et al. 1993). In the near-IR, at least a dozen point sources are found within the 10″ × 5″ region of bright IR emission from IRS 2 (Goldader & Wynn-Williams 1994).

The two blended mid-IR sources in W51 IRS 2 East and W51 IRS 2 West, are now resolved into at least five distinct peaks (Fig. 1). IRS 2 W is resolved into two extended sources, KJD 1 and KJD 2.[3] KJD 1, the westernmost, appears to be associated with the shell-like H II region W51d (Gaume et al. 1993). KJD 2 is elongated east-west and does not correspond to any radio continuum features. IRS 2 E is resolved into three compact sources, and a fourth compact source is detected for the first time ~5″ east (sources KJD 3/4/5/7). The IRS 2 complex is surrounded by an envelope of emission that extends roughly 10″–20″ around the compact sources. No compact source is detected at the position of the NH_3 (8, 9) maser and radio continuum source W51d2 (Gaume et al. 1993), although a compact source with $F(12.5\ \mu m) < 1.3$ Jy and $F(20.6\ \mu m) < 5.5$ Jy could be masked by the extended envelope. Based on the brightness of the envelope at the position of the NH_3 (3, 3) maser, upper limits of 0.03 and 0.17 Jy at 12.5 and 20.6 μm, respectively, can be placed for a compact source at that location as well. Four additional compact sources were detected at 12.5 and 20.6 μm KJD 8/9/10/11, to the east of IRS 2, but since they were below the sensitivity of the CVF observations, they will not be discussed further.

[3] The mid-IR sources described here are designated KJD 1 through 11, in order of increasing R.A.

TABLE 4

SOURCE POSITIONS

Source		Offset Δα	Offset Δδ	R.A. (J2000)	Decl. (J2000)	Compact (c)/Extended (e)[a]
W51 IRS 2.....	KJD 1	−3.2	+1.9	19 23 39.96	14 31 8.0	e
	KJD 2	−1.7	+1.2	19 23 40.06	14 31 7.3	e
	KJD 3	+0.0	+0.0	19 23 40.18	14 31 6.1	c
	KJD 4	+0.8	+1.6	19 23 40.24	14 31 7.7	c
	KJD 5	+1.1	+0.5	19 23 40.26	14 31 6.6	c
	KJD 6	+3.5	+5.5	19 23 40.21	14 31 11.6	c[b]
	KJD 7	+5.2	−0.3	19 23 40.54	14 31 5.8	c
	KJD 8	+6.5	−5.3	19 23 40.63	14 31 0.8	c[b]
	KJD 9	+11.7	+0.5	19 23 40.99	14 31 6.6	c[b]
	KJD 10	+12.5	−2.1	19 23 41.04	14 31 4.0	c[b]
	KJD 11	+16.1	+5.3	19 23 41.29	14 31 11.4	c[b]
Mon R2.....	IRS 1	+4.6	−11.5	06 07 45.98	−06 23 04.1	e
	IRS 2	+0.0	+0.0	06 07 45.67	−06 22 52.6	c
	IRS 5	−2.6	+13.9	06 07 45.50	−06 22 38.7	c
	[AW 90] a_i	+11.3	+15.8	06 07 46.42	−06 22 36.9	c
DR 21.....	N	+0.0	+0.0	20 39 1.26	42 19 53.4	c
	S	−8.2	−13.3	20 39 0.52	42 19 40.1	e
S140.....	IRS 1	+0.0	+0.0	22 19 18.21	63 18 46.9	c
	IRS 2	−0.5	+17.1	22 19 18.14	63 19 12.8	c
	IRS 3	+10.2	+2.9	22 19 19.72	63 18 49.8	c
	VLA 4	−4.8	−6.3	22 19 17.50	63 18 40.6	e

[a] Compact (c) sources are essentially point sources, although they might be slightly extended relative to the standard star (Table 1). Extended (e) sources are either distinctly elongated (W51 IRS 2 KJD 1 and 2) or have no well-defined peak (Mon R2 IRS 1, DR 21 S, S140 VLA 4). Relative positional errors for the compact sources are estimated to be less than 1″. Those for the extended sources will necessarily be higher.

[b] These are the five additional compact sources detected in W51 IRS 2 mentioned in the text.

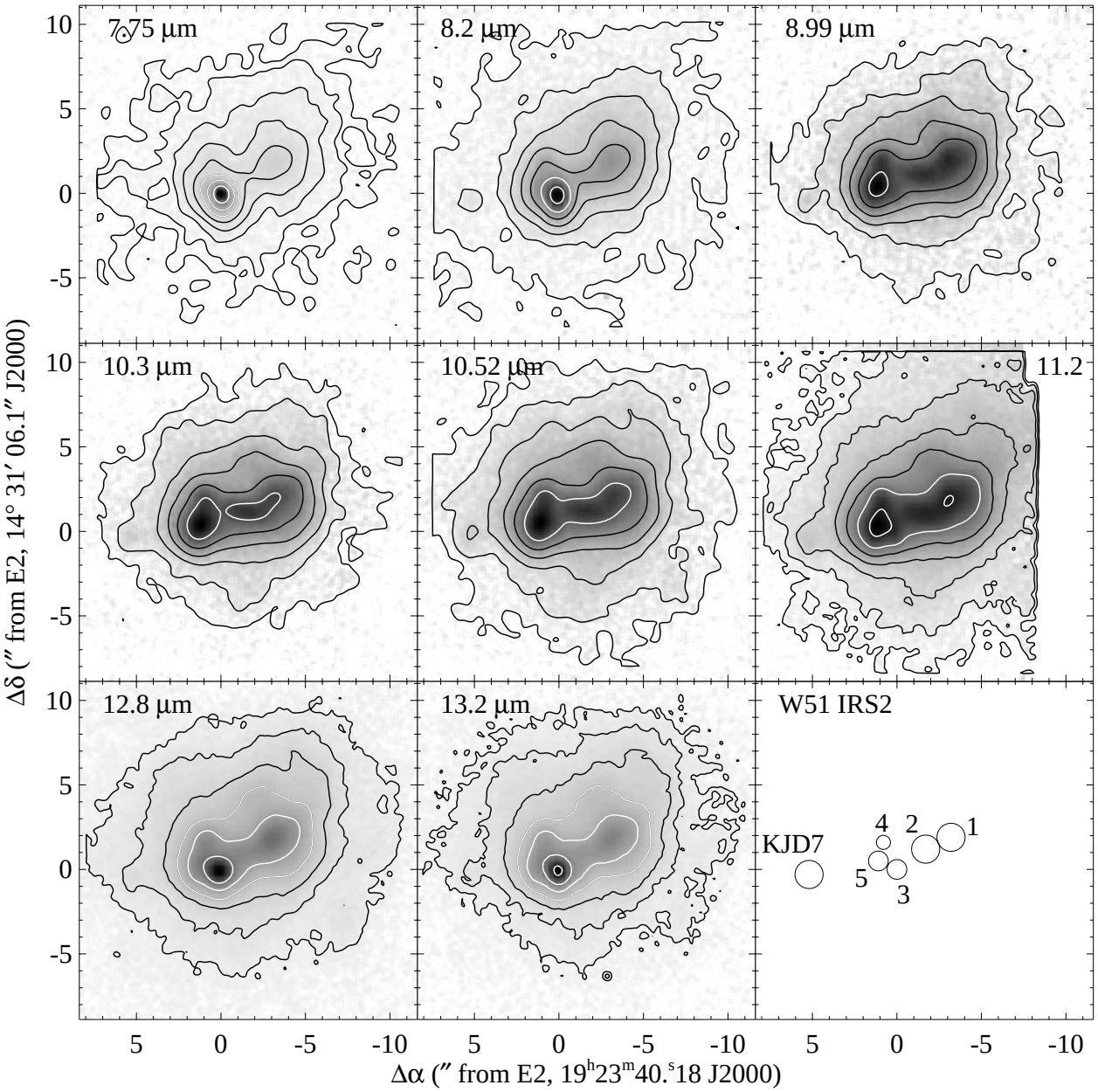

FIG. 1.—W51 IRS 2 with the MIRAC3 CVF. Source positions and aperture sizes used for photometry are shown in the lower right-hand panel (see text). The flux scale is $-3.1 < \log F < -0.5$ Jy, where darker is more intense. Contours, smoothed to 1″.1, are logarithmic, at 0.1, 0.2, 0.4, …, 25.6×10^{-2} Jy, except in the 12.8 and 13.2 μm images, where the lowest contour level is 0.4×10^{-2} Jy.

Figure 2 shows the 12.5/20.6 μm color temperature and 12.5 μm opacity maps. The hottest dust $T_d \sim 225$ K lies south and southwest of source KJD 3, and extends to the northwest. Some of the compact sources correspond to relatively cool ($T_d \sim 140$–160 K), high-opacity clumps, such as KJD 4 and KJD 7. An additional compact source, KJD 6, lost in the extended emission, is tentatively detected about 7″ northeast of KJD 4 as a temperature minimum and opacity peak. KJD 5 corresponds to a high-opacity clump, but not any particular temperature feature. KJD 1, although at a minimum in the temperature distribution, still corresponds to the hot $T_d \sim 190$ K, high-opacity dust associated with H II regions. KJD 2 corresponds to a slight opacity enhancement, but no feature in the temperature map.

Because the mid-IR emission is optically thin (Table 3), the dust mass can be estimated. Following Hildebrand (1983) and Natta & Panagia (1976), the mass in hot dust grains is

$$M_d(\mathrm{hot}) = \frac{F_\nu}{B_\nu(\overline{T})} \frac{4}{3} D^2 \frac{a\rho}{Q_e}, \quad (1)$$

where F_ν is the measured flux, $B_\nu(\overline{T})$ is the blackbody flux at temperature $\overline{T}$, and D is the distance to the star-forming cloud. The dust parameters are the grain mass density $\rho \sim 2$ g cm^{-2}, the characteristic grain size $a \sim 0.01$ μm, and the grain emissivity $Q_e \sim 10^{-4}$ (Becklin et al. 1976). With the 12.5 μm fluxes and 12.5/20.6 μm color temperatures from Table 3, this gives hot dust masses of $M_d \sim 5 \times 10^{-4}$ $M_\odot$.

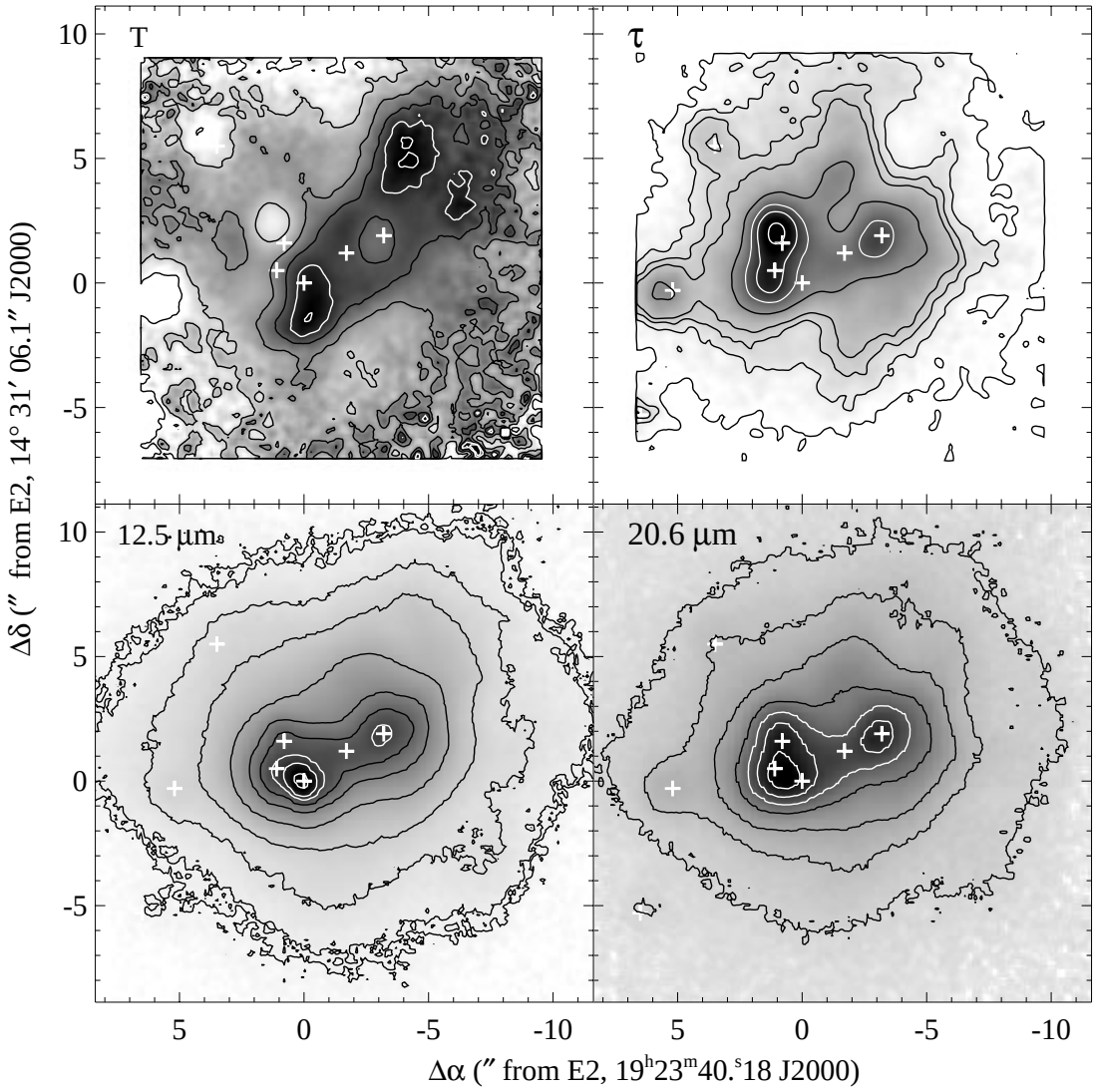

FIG. 2.—W51 IRS 2 color temperature map (*upper left*; $133 < T_d < 180$ K, contours at 130, 140, 150, 160, 170, and 180 K) and opacity map (*upper right*; $-2.5 < \log \tau_{12.5} < -1.2$, contours at 0.25, 0.5, 0.75, 1.0, 2.0, 3.5, 5.0, and 7.5×10^{-2}). Darker is hotter or more opaque, as appropriate. Though just tentatively detected at 8–13 μm, KJD 7 is readily apparent in the opacity map, and an additional cold opaque source, KJD 6, is tentatively detected at (+3.5, +5.5). Compact mid-IR sources are indicated with pluses. Also shown is the 12.5 μm map in the lower left ($-3.1 < \log F < -0.8$ Jy, contours at 0.2, 0.25, 0.5, 1.0, 2.5, 5.0, 7.5, 10.0, 12.5, and 17.5×10^{-2} Jy) The 20.6 μm map is in the lower right ($-4.0 < \log F < -0.57$ Jy, contours at 1.0, 2.5, 5.0, 10, 15, 20, and 25×10^{-2} Jy).

Larger, cooler grains that give rise to the FIR emission (e.g., Harvey et al. 1986) contribute about an order of magnitude more mass (e.g., Panagia 1975; Gezari et al. 1985). The standard gas-to-dust ratio of 100 (e.g., Whittet 1992; Mathis 1971) is then used to estimate the gas mass for each source in the given aperture. The total mass in hot dust in IRS 2 is roughly $M_d(\text{hot}) \approx 0.6\, M_\odot$.

A rough estimate of the gas density can also be made by using the aperture size as the physical size and assuming spherical symmetry. This calculation gives densities of $n_{\text{gas}} \sim 10^5$–10^6 cm^{-3}. These densities are comparable to clumps of similar size (a few hundredths of a parsec) found through dense gas tracers such as NH_3 (e.g., Orion-KL, Migenes et al. 1989) and CS (e.g., S140, Hayashi & Murata 1992) in typical massive star-forming regions. The densities in the cores are enhanced by factors of 3–30 relative to the mean gas density in IRS 2 calculated in this fashion. The dust mass and gas densities are included in Table 3.

Caution must be used in associating the sources in IRS 2 E with sources at other wavelengths due to the extremely deep silicate absorption (§ 4) associated with source KJD 3. As remarked in § 2, KJD 5 is the brightest source at $\lambda \sim 9$–11 μm, and again at 20 μm, whereas KJD 3 dominates at the other mid-IR wavelengths. With the assumption that KJD 3 corresponds to the 8 μm peak of Genzel et al. (1982), sources KJD 4 and KJD 5 appear to correspond to the double-lobed 3.6 cm structure of d1, albeit with a $\sim 0\farcs5$ offset in R.A., well within the 1″ error bars of the Genzel et al. (1982) coordinates. KJD 1 lies slightly east of the center of the shell-like 3.6 cm structure of radio source d (Gaume et al. 1993), where the radio shell is brighter and more complete.

3.2. *Mon R2*

The massive star formation region Mon R2 lies at a distance of 950 pc (Wolf, Lada, & Bally 1990). It is associated

with optical reflection nebulosity, a compact H II region with extended radio structure (Downes et al. 1975; Massi, Felli, & Simon 1985), H_2O and OH masers, and bright near-IR emission from numerous compact and extended sources. The spectacular IR ring, first detected by Hackwell et al. (1982) at 10 and 20 μm, is associated with strong "centrosymmetric" K-band polarization (Aspin & Walther 1990; Yao et al. 1997).

Five point sources were detected in the 45″ × 45″ region centered on Mon R2 IRS 2, including IRS 1, IRS 2, IRS 3 (saturated, at the eastern edge of the field), IRS 5, and (AW90) a_i (Fig. 3). Diffuse emission in the large ringlike structure was also detected at several wavelengths. At 20.6 μm and at 7.75, 8.2, and 11.2 μm with the CVF, the diffuse emission is well-correlated with the near-IR emission (e.g., Howard, Pipher, & Forrest 1994; Yao et al. 1997). At 12.8 μm, on the other hand, the diffuse emission lies almost completely within the ring and is likely tracing [Ne II] in the H II region ionized by IRS 1.

The compact source IRS 2 dominates the dust color temperature (12.5 μm/20.6 μm) map (Fig. 4) at $T_d \sim 385$ K, with the temperature peaks at IRS 1 and 5 reaching $T_d \sim 170$ K and $T_d \sim 160$ K, respectively. The dust in the ring has a relatively uniform temperature of $T_d \sim 100$–115 K. In contrast, the 12.5 μm opacity (Fig. 4) is concentrated strongly in the ring, reaching values of $\tau_{12.5} \sim 0.01$–0.04 just southeast

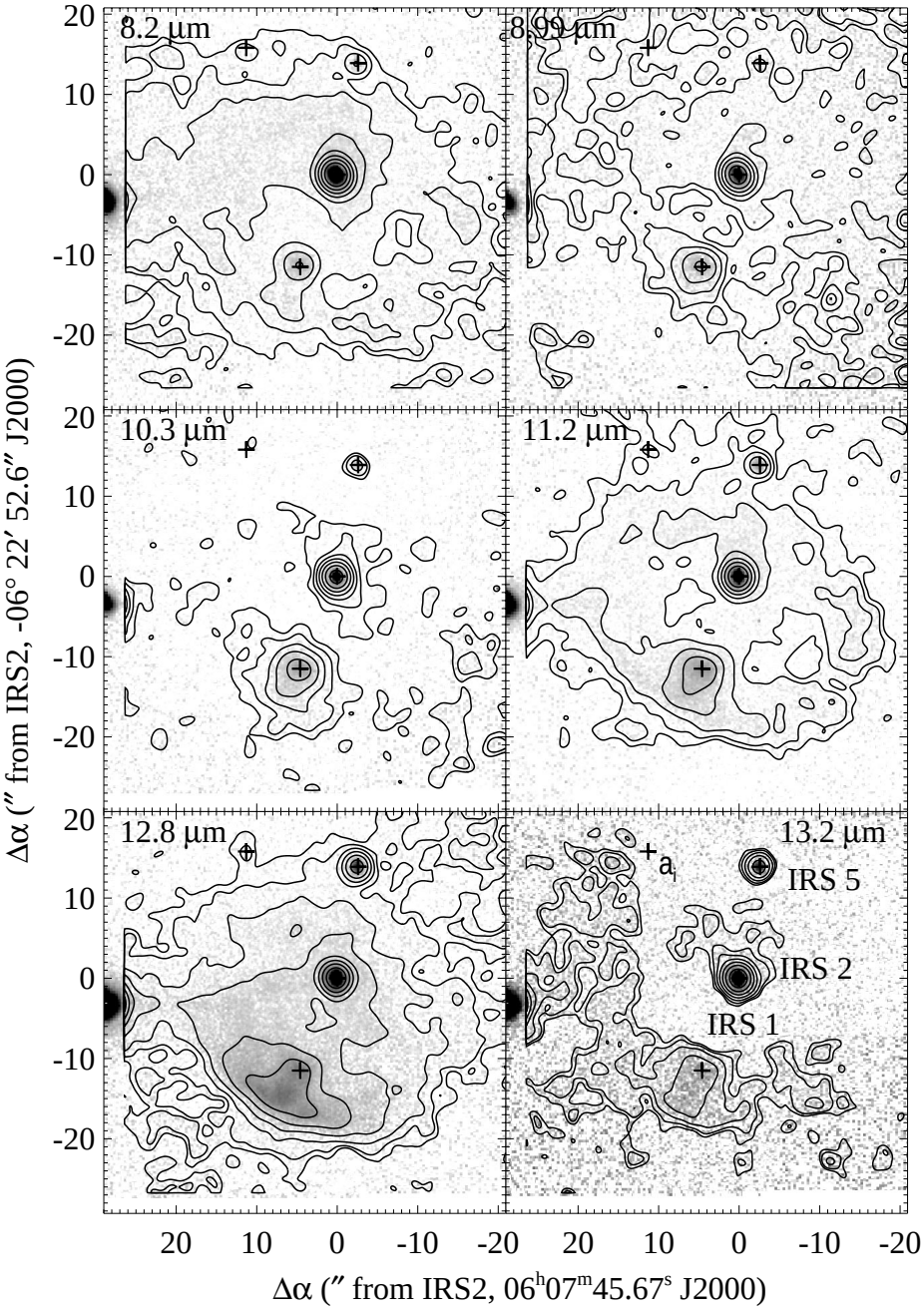

FIG. 3.—Mon R2 with the MIRAC3 CVF. The flux scale is $-3.1 < \log F < -1.3$ Jy, where darker is more intense; IRS 2, at (0, 0), is saturated on this scale at all wavelengths. Contours, smoothed to 2″, are logarithmic, at 0.25, 0.5, 1.0, 2.0, …, 64 × 10^{-3} Jy (except at 13.2 μm, where the lowest level is 0.5 × 10^{-3} Jy). IRS 1, 2, 5, and a_i are indicated with pluses, and labeled in the lower right-hand panel. The bright source off the east edge of the field is IRS 3, at (+30, −3).

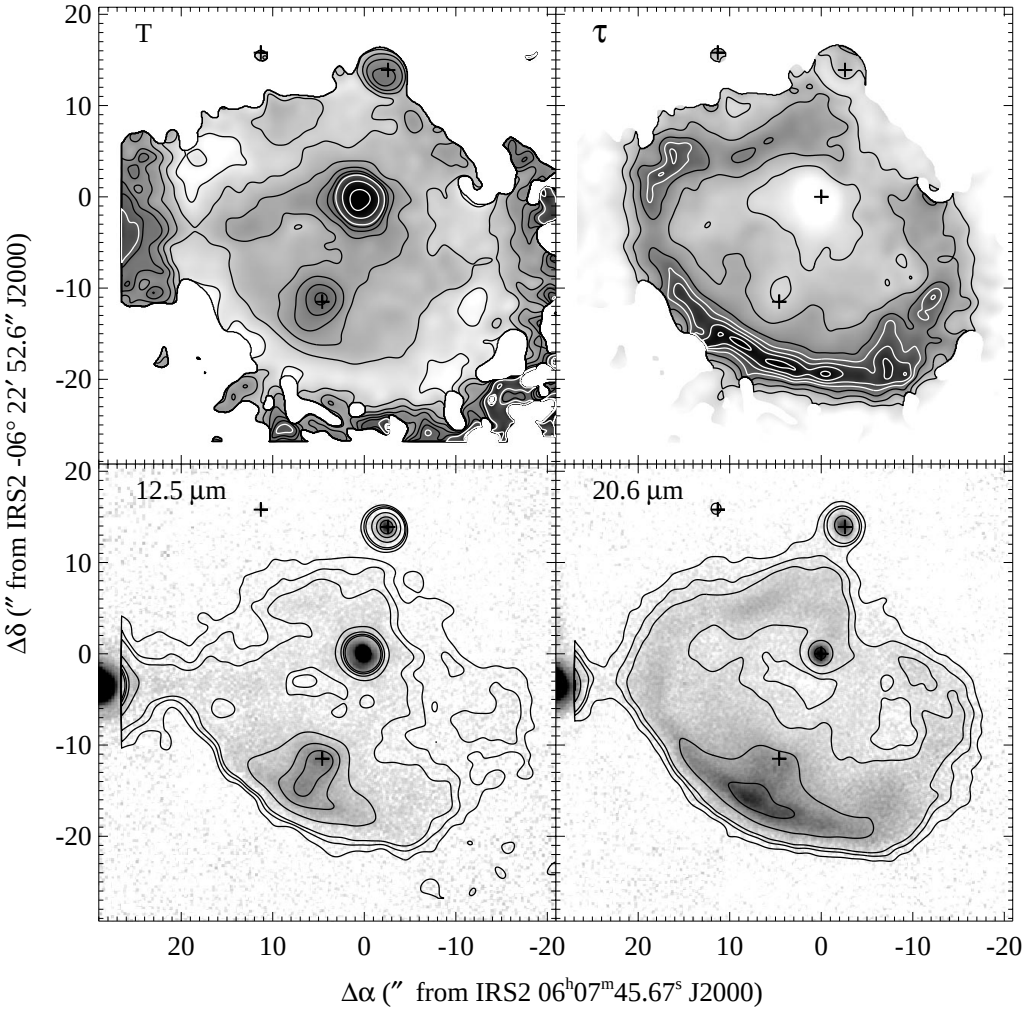

FIG. 4.—Mon R2 color temperature map (*upper left*; $87 < T_d < 250$ K, contours at 80, 90, 100, 110, 120, 130, 140, 150, 200, and 250 K) and opacity map (*upper right*; $-2.9 < \log \tau_{12.5} < -0.8$, contours at 1.0, 2.5, 5.0, 7.5, 10.0, 12.5, and 15×10^{-2}). Darker is hotter or more opaque, as appropriate. Also shown are the 12.5 μm data (*lower left*; $-3.2 < \log F < -1.4$ Jy, contours, smoothed to 2″, at 0.5, 0.75, 1.0, 2.5, 5.0, 7.5, 10, 50×10^{-3} Jy) and the 20.6 μm data (*lower right*; $-2.4 < \log F < -1.0$ Jy, contours, smoothed to 2″, at 0.5, 0.75, 1.0, 2.5, and 5.0×10^{-2} Jy). IRS 2, 3, and 5 are saturated at both wavelengths. (The ringlike structures around IRS 2 and 5 in the opacity and temperature maps are artifacts due to the beam-matching process.) IRS 1, 2, 5, and a_i are indicated with pluses.

of IRS 1. The opacity toward the point sources, on the other hand, is dramatically lower: $\tau_{12.5} \sim 0.003$ at IRS 1, $\tau_{12.5} \sim 0.004$, at IRS 2, and $\tau_{12.5} \sim 0.006$ at IRS 5.

As with W51 IRS 2, mass and densities were calculated for the three brightest compact sources IRS 1, 2, and 5, and for the 20 μm peak in the ring southeast of IRS 1 (Table 3). Massi et al. (1985) suggested a blister-type structure for the Mon R2 H II region confined by dense gas to the southeast, but allowed to expand more freely to the northwest. The fact that the gas in the ring is significantly denser than that toward the compact sources ($n_g \sim 10^7$ cm^{-3} as opposed to $n_g \sim 10^5$–10^6 cm^{-3}) directly supports the blister scenario.

3.3. *DR 21*

The DR 21 massive star-forming region lies approximately 3 kpc (Campbell et al. 1982; Pipenbrink & Wendker 1988) away in the Cygnus-X region. Radio observations show that the site consists of four compact H II regions, [RGG89] A, B, C, and D (e.g., Harris 1973; Dickel et al. 1986; Roelfsema et al. 1989). Additional indications of active star formation in this region include a large-scale, highly energetic, molecular outflow (e.g., Fisher et al. 1985; Wilson & Mauersberger 1990; Garden & Carlstrom 1992), shock-excited H_2 (Garden et al. 1986; Davis & Smith 1996), bright emission from PDR tracers such as [O I] 63 μm and [C II] 158 μm (Poglitsch et al. 1996; Lane et al. 1990), methanol (Plambeck & Menten 1990; Slysh et al. 1999), and H_2O (Palagi et al. 1993) masers, and high-luminosity far-IR emission ($L \sim 5 \times 10^5$ $L_\odot$, e.g., Campbell et al. 1982; Harvey et al. 1986; Roelfsema et al. 1989), mid-IR emission (Harvey et al. 1986), and near-IR emission (e.g., Roelfsema et al. 1989; Garden et al. 1990; Davis & Smith 1996).

The mid-IR emission from the core of DR 21 consists primarily of two bright sources of extended emission (Fig. 5), sometimes referred to as DR 21 N and DR 21 S (Wynn-Williams et al. 1974). The more compact source, DR 21 N, is associated with the radio continuum source [RGG89] D (Roelfsema et al. 1989), and the more extended source, DR 21 S, lies slightly northwest of the three radio sources [RGG89] A, B, and C. Faint extended sources are detected at 20.6 μm and in the convolved 12.5 μm data but are below the sensitivity limits at other wavelengths: 9″ west-northwest of DR 21 N, 10″ east-southeast of N, and 10″ east-southeast of DR 21 S. The mid-IR is morphologically

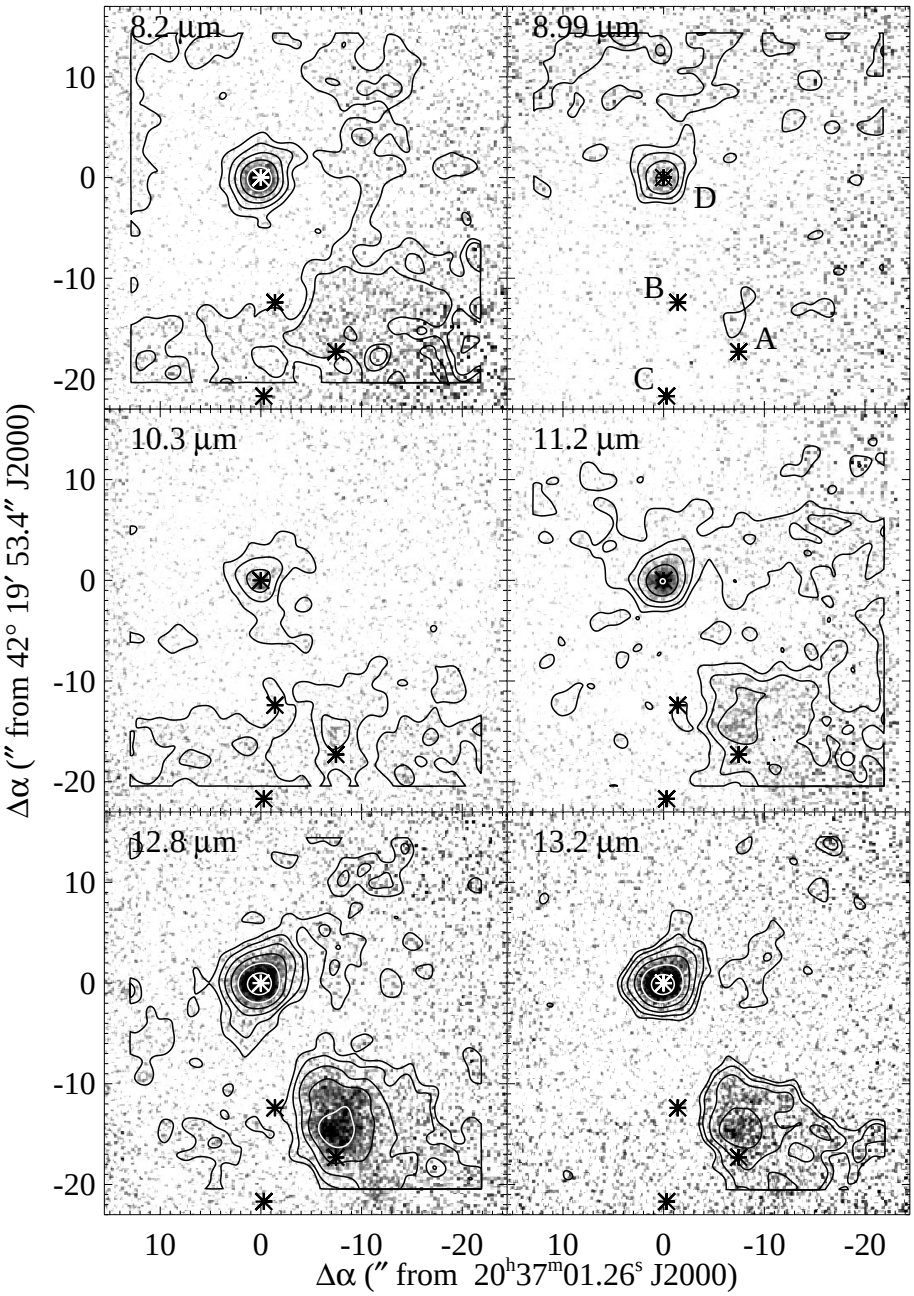

FIG. 5.—DR 21 with the MIRAC3 CVF. The flux scale is $-2.8 < \log F < -1.8$ Jy, where darker is more intense. Contours, smoothed to 2″, are at 0.25, 0.5, 1.0, 2.0, 4.0, and 8×10^{-3} Jy. Radio continuum sources [RGG89] A, B, C, and D are marked with asterisks and labeled in the 8.99 μm image (*top right*).

very similar to the 4.0 μm emission mapped by Roelfsema et al. (1989), including the faint extended structure.

DR 21 N dominates the color temperature map (Fig. 6) at $T_d \sim 195$ K, but shows only a moderate 12.5 μm optical depth $\tau_{12.5} \sim 0.0011$, which is consistent with the suggestion of Roelfsema et al. (1989) that the H II region contains little dust. DR 21 S is warmer toward the H II regions, starting at $T_d \sim 110$ K in the ridge on the northwest side, rising to $T_d \sim 155$ K near [RGG89] A, and finally peaking at almost $T_d \sim 200$ K in the southeast, nearer [RGG89] B and C. The 12.5 μm opacity map (Fig. 6) shows the cool ridge has high optical depth, whereas the opacity near the H II regions is smaller. We suggest that DR 21 S is not self-luminous, but is heated by radiation from the nearby H II regions to the southeast, particularly by [RGG89] A.

Roelfsema et al. (1989) suggested that at least half of the 4.0 μm continuum emission could be explained by free-free emission from the H II regions. Given the similarity in morphology between the 4.0 μm emission and the mid-IR images presented here, the free-free contribution at 12.5 and 20.6 μm should be calculated. Under the assumption of optically thin emission and the Rayleigh-Jeans approximation, the flux scales as $S_\nu \propto \nu^{-0.1}$ or $S_{\text{mid-}IR} \sim 0.5 S_{\text{radio}}$. Roelfsema et al. (1989) measure $\sim$2 Jy from [RGG89] D and a total of $\sim$12 Jy from [RGG89] A, B, and C, in 5″ apertures at both 4.9 and 14.7 GHz. The free-free contribution at mid-IR wavelengths will therefore be $\sim$1 Jy at DR 21 N and $\sim$6 Jy at DR 21 S. In 5″ apertures, DR 21 N has 17 and 41 Jy at 12.5 and 20.6 μm, respectively, and DR 21 S has 8 and 42 Jy. Thus, in DR 21 S, free-free emission can

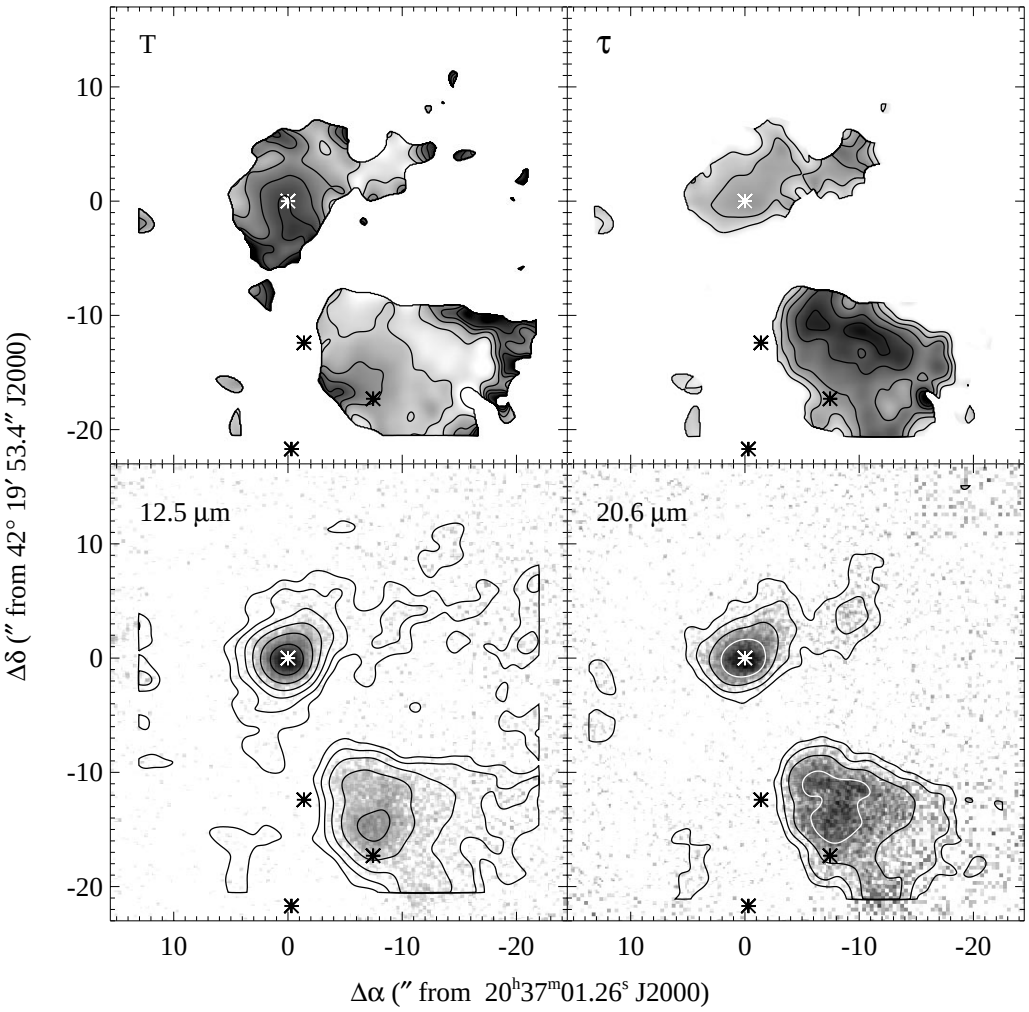

FIG. 6.—DR 21 color temperature map (*upper left*; $105 < T_d < 200$ K, contours at 100, 115, 130, 145, and 160 K) and opacity map (*upper right*; $-3.3 < \log \tau_{12.5} < -1.7$, contours at 0.1, 0.25, 0.5, 1.0, and 1.5×10^{-2}). Darker is hotter or more opaque, as appropriate. Also shown are the 12.5 μm data (*lower left*; $-3.1 < \log F < -1.8$ Jy, contours, smoothed to 2″, are logarithmic, at 0.2, 0.4, …, 6.4×10^{-3} Jy) and the 20.6 μm data (*lower right*; $-2.6 < \log F < -1.5$ Jy, contours, smoothed to 2″, are logarithmic, at 1.6, 3.2, 6.4, 12.8×10^{-3} Jy). Radio continuum sources [RGG89] A, B, C, and D are marked with asterisks.

account for ~75% of the emission at 12.5 μm, but only ~15% at 20.6 μm. If the 12.5 μm is indeed simply free-free emission from the H II regions, the difference in morphology between the radio and mid-IR continuum emission must be examined. One possible explanation is that the H II region spatially coincident with the mid-IR emission is sufficiently optically thick that the radio continuum emission is below the detection limits of Roelfsema et al. (1989). Another possibility is that high extinction toward the H II regions [RGG89] A, B, and C has suppressed the mid-IR emission. Roelfsema et al. (1989) suggest that the extinction is both high and patchy. However, the extinction to suppress mid-IR emission below our detection level exceeds even the $A_v \sim 100$–175 estimated by Roelfsema et al. (1989).

Toward DR 21 N, on the other hand, free-free emission contributes no more than ~2%–6% at either wavelength. Since the free-free contribution is negligible at DR 21 N, there must be dust nearby, either in a shell outside the H II region or in the H II region itself. This suggests that although the dust is optically thin, neglecting it entirely, in extinction estimates, for example (Roelfsema et al. 1989), is not justified for DR 21 N.

3.4. *S140*

S140 is a nearby (910 pc; Crampton & Fischer 1974) massive star-forming region with an edge-on PDR. The complex consists of an optically bright arc-shaped ionization front illuminated from the southwest by a B0 star HD 211880, and several additional B stars forming in the dense molecular core on the opposite side of the ionization front (e.g., Blair et al. 1978; Hackwell et al. 1982; Evans et al. 1989). The three previously known infrared sources in the core, IRS 1, 2, and 3 (e.g., Beichman et al. 1979; Hackwell et al. 1982) have radio fluxes consistent with zero-age main-sequence (ZAMS) spectral types of B1.5–B2 (Evans et al. 1989). Two additional radio sources in the core, (SFC 83) S140 4, known as VLA 4, and (BBW 79) S140 NW, have ZAMS spectral types of B2–B3 (Evans et al. 1989). The core also contains methanol (Slysh et al. 1999) and H_2O masers (Genzel & Downes 1979) and a high-velocity molecular outflow centered on IRS 1 (e.g., Blair et al. 1978; Hayashi et al. 1987).

Figure 7 shows the mid-IR emission from the S140 star-forming core. The three previously known infrared sources, IRS 1, 2, and 3 (Hackwell et al. 1982) are detected at most

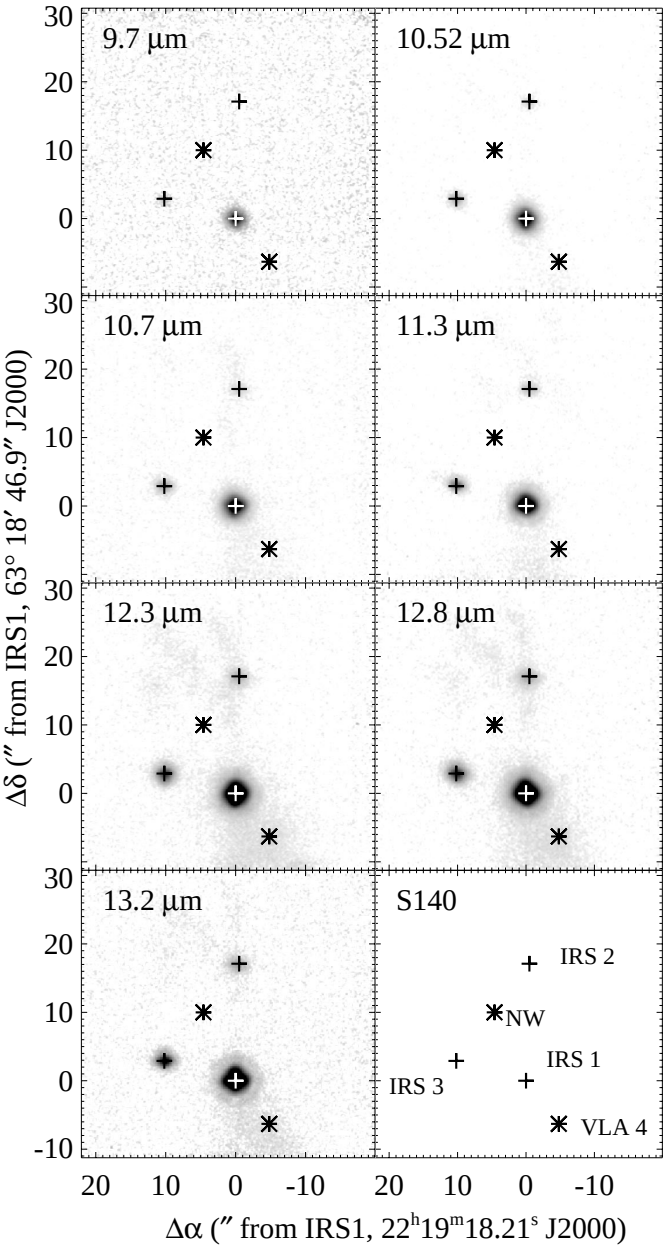

FIG. 7.—S140 with the MIRAC3 CVF. The flux scale is $-2.9 < \log F < -0.8$ Jy, where darker is more intense. IRS 1, 2, and 3 are marked with pluses, VLA 4 and NW are marked with asterisks, and labels are in the lower right-hand panel. IRS 1 is saturated at all wavelengths, as is IRS 3 at 13.2 μm.

wavelengths. The radio continuum source VLA 4 (Simon et al. 1983; Evans et al. 1989) has been detected in the mid-infrared for the first time. Two compact sources are tentatively detected at 20.6 μm to the north of IRS 2 and the northeast of IRS 3, as is source NW (Fig. 8). The source northeast of IRS 3 may be the mid-IR counterpart of a source apparent in the H- and K_s-band images of Yao et al. (1998), and is labeled IRS 6[4] in Figure 8. It also appears in the 20 μm images of Hackwell et al. (1982), although it was not noted in their discussion. Like IRS 2 itself, the new northern source, labeled IRS 7 in Figure 8, does not have a near-IR counterpart. Interpretation of the S140 data is complicated by the presence of an internal reflection responsible for much of the extended structure visible in the CVF images near IRS 2 (the narrowband data at 12.5 and 20.6 μm were not affected by this problem).

The color temperature and opacity distributions are shown in Figure 8. The strong infrared sources IRS 1, 2, and 3 are peaks in both color temperature and dust opacity, with IRS 2 the coldest and most opaque of the three. The newly detected sources north of IRS 2 and northwest of IRS 3 are opacity peaks but have no corresponding temperature feature. On the other hand, the weak radio sources, VLA 4 and VLA NW, correspond to temperature minima and weak opacity peaks.

4. DISCUSSION: SILICATE ABSORPTION

4.1. *Disks around Massive Stars?*

In each massive star-forming region, at least one sources shows deep silicate absorption in its spectral energy distribution (Fig. 9). Previous observations of massive star-forming regions have shown silicate absorption, but were unable to distinguish whether the absorbing material was local to the massive young star or part of the cloud in which it was embedded. For at least two of the massive star-forming regions observed here, the absorbing material must be highly localized and not a global property of the parent cloud or other intervening material. In W51 IRS 2, for example, the silicate absorption is associated with only one (KJD 3) of the five compact sources that have now been resolved. Similarly, in Mon R2, and in NGC 6334I (Kraemer et al. 1999a), two of three and one of four compact sources, respectively, have silicate absorption. A natural explanation for a localized silicate absorption feature is circumstellar material, such as the protostellar disks or shells observed around lower mass young stellar objects. Indeed, Adams (1993) suggests that accretion via a circumstellar disk is required to overcome the large radiation pressure (which could otherwise disrupt the infall of material) inherent in forming high-mass stars.

Recently, theoretical models of the radiative transfer through protostellar disks have begun to include emission and absorption from silicate grains at 10 μm (e.g., Sonnhalter, Preibisch, & Yorke 1995; Men'shchikov & Henning 1997). Their standard models suggest that circumstellar disks must be viewed with inclinations less than 10° (Men'shchikov & Henning 1997) to 20° (Sonnhalter et al. 1995) of edge-on for the silicate feature to be seen in absorption. For a random distribution of viewing angles, roughly 10%–20% of young stars with disks have sufficiently high optical depths at 10 μm to show silicate absorption. In the three massive star-forming regions where the silicate absorption is clearly local (W51 IRS 2, Mon R2, and NGC 6334I), and therefore potentially disk-produced, four of twelve, or 33%, of the compact sources show the absorption feature. If the absorption features detected in DR 21, S140, and W49 (Smith et al. 2000) are also localized, this percentage goes even higher. In addition to the viewing angle, other influences on the optical depth of the silicate feature include the "flare" or opening angle of the disk, the ratio of the disk thickness to its diameter, the disk mass and size, and the properties of the dust grains. Although the fraction of

[4] The labels IRS 6 and 7 are assigned to the new sources as an extension of the original nomenclature of Beichman et al. (1979). Simon et al. (1983) used 4 and 5 to denote radio sources, of which VLA 4 now has an infrared counterpart.

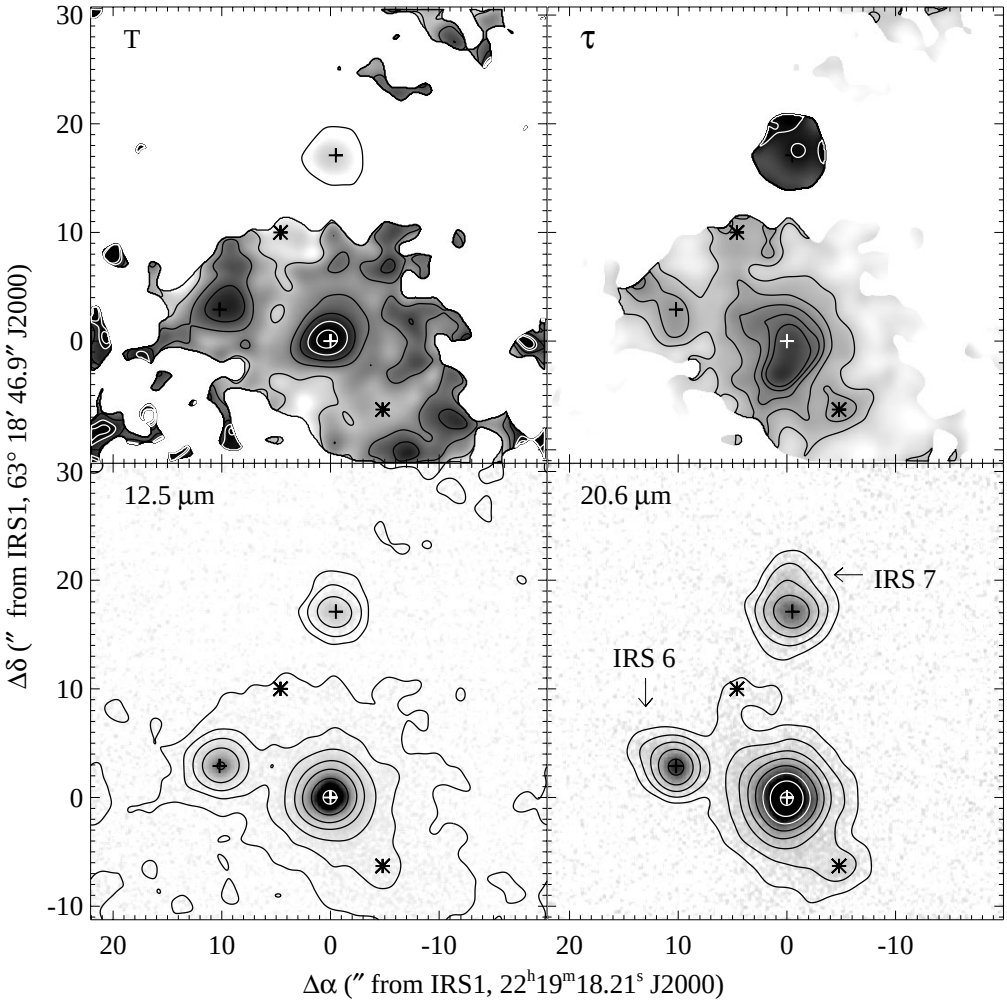

FIG. 8.—S140 color temperature (*upper left*) and opacity (*upper right*) maps. Darker is hotter or more opaque, as appropriate. Also shown are the 12.5 μm data (*lower left*) and the 20.6 μm data (*lower right*; $-2.6 < \log F < -0.8$ Jy; IRS 1 is saturated to show the fainter emission). The 20.6 μm contours, smoothed to 2″, are logarithmic, at 0.4, 0.8, …, 51.2×10^{-2} Jy. Scales for the temperature and opacity maps, and contour intervals for the 12.5 μm map are not given owing to the problematic flux calibration of the 12.5 μm data (see text). The new sources IRS 6 and 7 are indicated by arrows in the 20.6 μm image; other symbols are as in Fig. 7.

massive star-forming sites with silicate absorption seems high compared to the standard disk models, appropriate adjustment of these parameters can account for the relatively high numbers. Also, silicate absorption due to other local causes such as circumstellar shells could increase the fraction of sources in which the feature is observed.

4.2. *Characterizing the Silicate Absorption Feature*

The template to which most silicate features are compared is the Trapezium emissivity (Forrest, Gillet, & Stein 1975; Hanner, Brooke, & Tokunaga 1995) from the strong silicate emission feature toward the Trapezium H II region in Orion. The Trapezium emissivity is well-characterized as single-temperature (250 K), optically-thin emission, and has been used to describe the silicate emission and absorption features toward many young low-mass stars. Two common models were fitted to the compact sources with complete data across the absorption feature (after Hanner et al. 1995):

$$F = \frac{a_0}{\lambda}\left(\frac{\lambda}{9.7}\right)^m \epsilon_t(\lambda) e^{-\tau_{9.7}\,\epsilon_t(\lambda)} \text{ (thin)} , \qquad (2)$$

$$F = \frac{a_0}{\lambda}\left(\frac{\lambda}{9.7}\right)^m e^{-\tau_{9.7}\,\epsilon_t(\lambda)} \text{ (thick)} . \qquad (3)$$

Here $\tau_{9.7}$ is the dust optical depth at 9.7 μm, a_0 is a scaling factor, and m is a measure of the spectral index. The dust emissivity $\epsilon_t(\lambda)$ is the Trapezium emissivity, adapted from Hanner et al. (1995). This assumes that the absorbing dust has the same grain properties as the emitting dust in the Trapezium. The first equation describes optically thin emission obscured by cold foreground dust along the line of sight. The second describes optically thick emission with cold foreground dust. Neither model fits the data very well for any source, owing in part to the line emission present in the data which is not included in the models. The [Ne II] 12.8 μm line, in particular, has a line-to-continuum ratio of 3–5 toward DR 21, Mon R2, and W51 (based on *ISO*-SWS measurements; Kraemer et al. 2001). Despite these limitations, the optical depth $\tau_{9.7}$ can be constrained to approximately 2–5. This range is consistent with that observed around compact H II regions fitted with more complex dust models (Faison et al. 1998).

The fits did not converge for the sources with only data at $\lambda \gtrsim 10$ μm: S140 and W49 Q„ R, and S, probably because

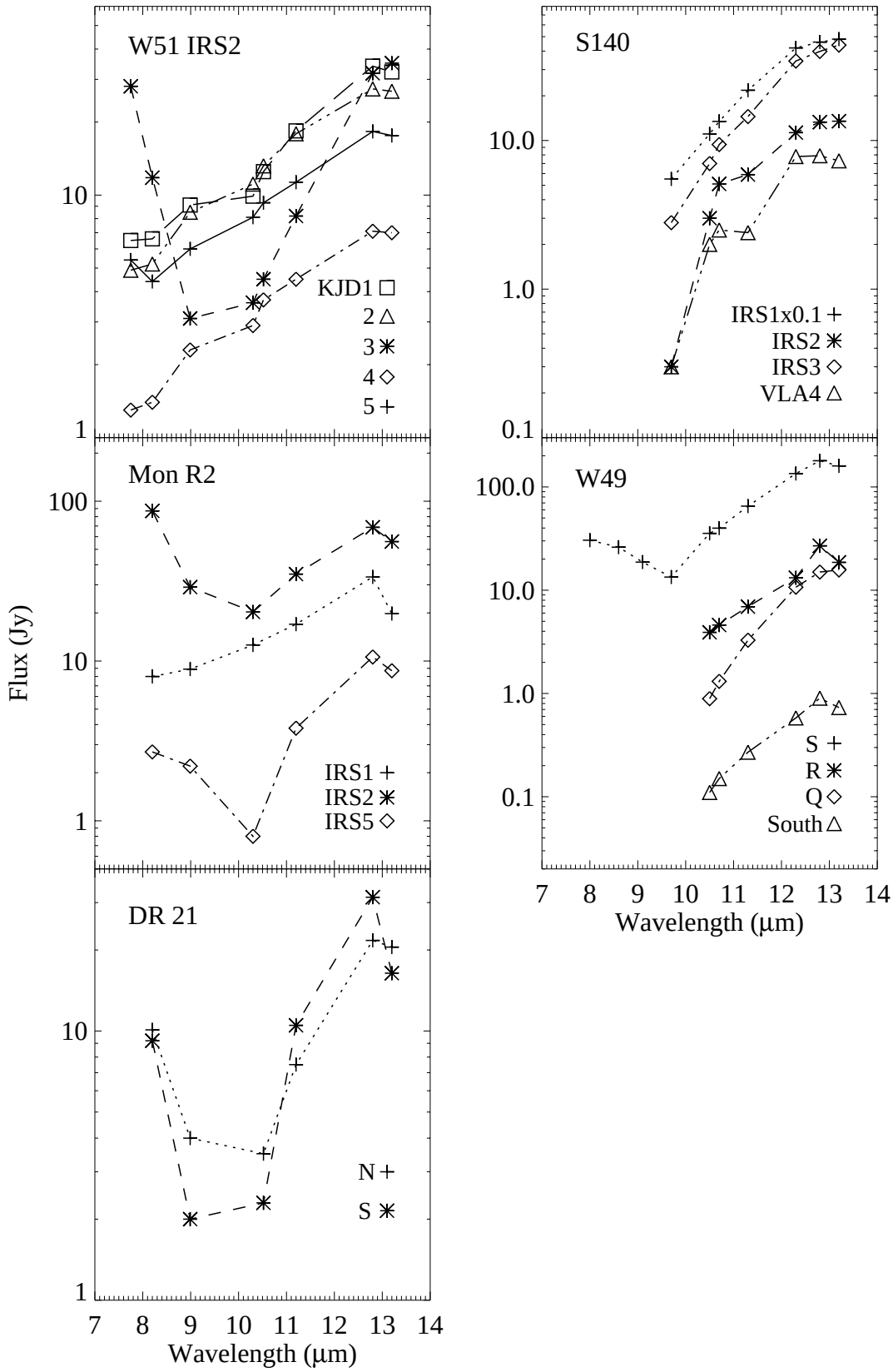

FIG. 9.—Spectral energy distributions. Aperture sizes as reported in Table 1. Data for W49 is from Smith et al. (2000).

too few data points were observed. A simple test was thus developed to determine the presence or absence of silicate absorption even in the absence of complete spectral information. An exponential function was fitted to the data for $\lambda \sim 10$–$13.2\ \mu$m:

$$F = be^{s\lambda}\ , \tag{4}$$

where s is a measure of the shape of the spectrum between

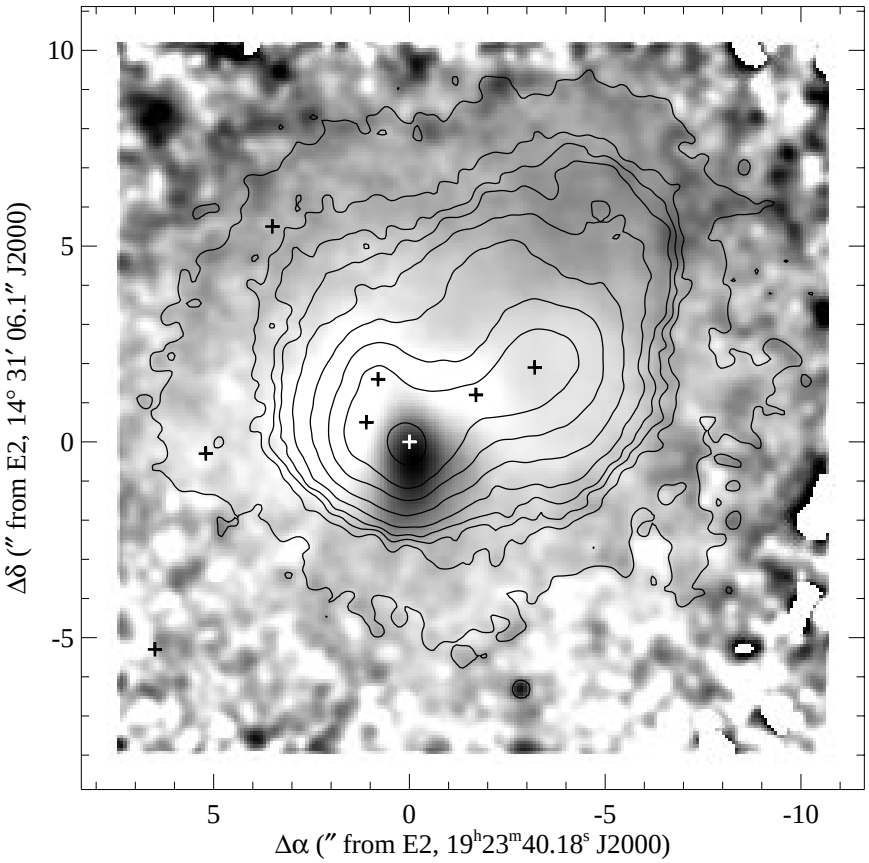

FIG. 10.—Silicate absorption distribution for W51 IRS 2 (*gray scale*; $0.2 < \log f < 0.95$). The 13.2 μm continuum emission is superposed (*contours*; smoothed to 1″.1). Compact mid-IR sources are indicated with pluses.

10 and 13 μm and b is a scaling factor. First, the sources with the complete wavelength coverage (8–13 μm) were fitted in this manner. Two distinct populations emerge: sources with clear silicate absorption (W51 IRS 2 KJD 3, W49 S, DR 21 N, DR S, Mon R2, and IRS 5) have $\bar{s} = 0.5$, whereas those without (Mon R2 IRS 1, the other compact sources in W51 IRS 2) have $\bar{s} = 0.3$. A Kolmogorov-Smirnov (KS) test suggests that there is less than a 3% probability that these two sets of sources are drawn from the same population. Sources without complete spectral data (S140, W49), the "unknowns," were then fitted. All of the compact sources in S140 and W49 have $s \sim 0.4$–0.7. A KS test was performed comparing the "unknown" sources to those with and without clear absorption, with KS probability factors of 0.54 and 0.02, respectively. Because of the small numbers of sources involved, the significance of this result was tested by removing each source in each data set and re-performing the KS test. The correlation between the "unknowns" and the no-absorption set remains poor: KS probability factors of 0.02–0.07. The KS probability factor between the "unknowns" and the absorption set ranged from 0.32 to 0.92, with more than half of the trials resulting in probabilities of greater than 0.6. We conclude, therefore, that the "unknowns" are significantly more likely to have silicate absorption present than not.

4.3. *Spatial Variations and Temperature/Opacity Comparisons*

Because the present data set consists of images, as opposed to single-beam pointed observations, the distribution of the absorbing silicates within the star-forming clouds can be examined. For each region, the 8.2 and 13.2 μm continuum maps were interpolated to form a pseudo-continuum map at 9.6 μm. After Gezari, Backman, & Werner (1998), these maps were then divided into the mean of the 8.99 and 10.3 μm maps, which roughly bracket the silicate feature. This creates a map of the so-called "trough depth" or "absorption factor" in each region (e.g., Jones et al. 1980; Arens et al. 1984; Gezari et al. 1998). The absorption factor f is approximately the ratio of the continuum to the depth of the silicate absorption feature at $\lambda \sim 9.6$ μm, and gives a lower limit to the strength of the feature. (This is only a lower limit because the feature strength generally peaks near $\lambda \sim 9.7$–9.8 μm, but the average wavelength of the 8.99 and 10.3 μm maps is 9.6 μm, 0.1–0.2 μm off the peak.) To increase the signal-to-noise of the extended emission in DR 21 and Mon R2, the data were convolved to 2″ prior to interpolation. Flux cutoffs of 0.2 mJy and 0.05 mJy were applied to DR 21 and Mon R2, respectively. W51 IRS 2 was convolved to 1″.1 and a 0.05 mJy cutoff was applied. The absorption factor maps can then be compared with the distribution of flux, color temperature, and 12.5 μm opacity in each source. A positive correlation between the 12.5 μm opacity and the absorption factor, for example, could indicate that the same population of grains produces both the silicate absorption and the 12.5 μm emission.

4.3.1. *W51 IRS 2*

Figure 10 shows the silicate absorption distribution compared with the 13.2 μm continuum emission in W51 IRS 2.

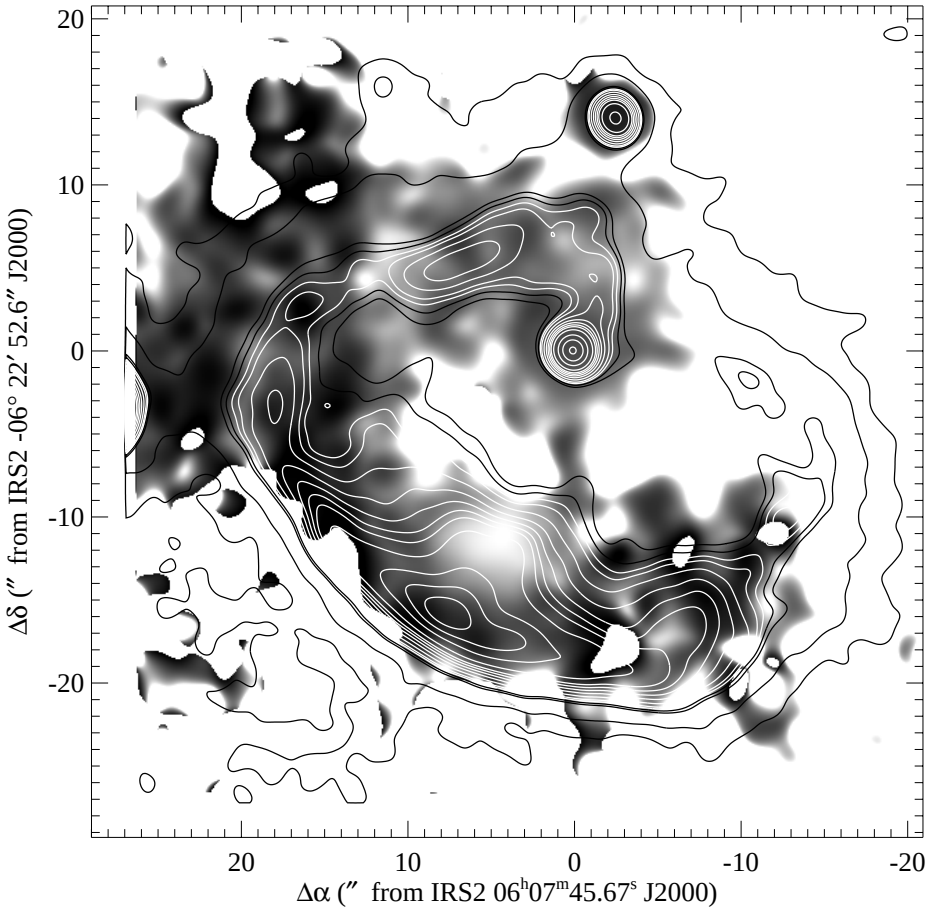

FIG. 11.—Silicate absorption distribution for Mon R2 (*gray scale*: $1 < f < 10$). The 20.6 μm continuum emission is superposed (*contours*; smoothed to 2″).

The most striking feature is the wedge-shaped structure of deep absorption that peaks near source KJD 3, where the absorption factor peaks at a value of $f \sim 8$. As was seen with the photometric measurements, the other compact sources lie in regions of little or no absorption. Sources KJD 2, KJD 4, and KJD 5 lie in a V-shaped region with a factor of $f \sim 1.0$–1.5. Source KJD 1 lies on a plateau of slightly higher absorption, $f \sim 1.8$–2.0. A region of even higher absorption, $f \sim 2.0$–3.5, extends to the northwest and seems to correspond a tongue of dust emission apparent in the individual CVF images (Fig. 1). The deep absorption near KJD 3 and that toward the northwest also correspond to the hottest color temperatures in the region. A similar phenomenon, with silicate extinction correlated with the hottest dust was observed in Orion toward IRc2 (Gezari et al. 1998).

The silicate absorption peak lies 2″ east of the 2 mm dust core (Zhang et al. 1998), and the NH_3 (3, 3) emission peak (Zhang & Ho 1995) lies an arcsecond southwest of KJD 3. The 2 mm continuum emission extends to the northwest, similar to the direction and shape of enhanced silicate absorption near source KJD 1. Further, the CS (3–2) emission (Zhang et al. 1998) is relatively sharp-edged to the northwest and northeast, with the same angle and orientation as the V-shaped absorption region of $f \sim 1.0$–1.5. We suggest that the core traced by the 2 mm dust and NH_3 (3, 3) emission is responsible for the silicate absorption at source KJD 3. Sources KJD 4 and KJD 5, and KJD 1, which correspond to the H II regions d1 and d, appear to be bounding the star formation activity to the east and northwest of IRS 2. The higher gas densities found for KJD 4 and KJD 5 relative to that at KJD 3 (§ 3.1, Table 3) supports this suggestion.

4.3.2. *Mon R2*

Figure 11 shows the distribution of silicate absorption in Mon R2, with the 20.6 μm flux shown in contours for comparison. As seen from the photometric measurements (Fig. 9), IRS 5 is a peak in the absorption factor ($f \sim 5$), IRS 2 has only a moderate feature ($f \sim 2.5$–3) and IRS 1 shows no absorption at all ($f \sim 1$). ([AW 90] a_i is below the flux cutoff and IRS 3 is off the edge of the field.) The emission ring shows highly varied absorption, $f \sim 1$–10, some (but not all) of which corresponds to morphological features seen at 20 μm. The southeastern arc, which coincides with the edge of the H II region (Massi et al. 1985), has a higher average absorption factor ($f \sim 5$) than the northwestern ($f \sim 1$) or northeastern arcs ($f \sim 2$). Small segments of the ring that are bright at 20 μm may (e.g., [+16, +2.5], [+3, −12]) or may not (e.g., [−6, −17], [+11, −5]) coincide with enhanced ($f > 1$) absorption features. In contrast to W51 IRS 2, the silicate absorption shows no correspondence with the temperature peaks. It corresponds more to the 12.5 μm opacity, so far as the ring stands out in both opacity and absorption factor, but that too is not a one-to-one correspondence. The compact sources have no simple correspondence, as they rank from highest to lowest: IRS 2, 1, 5 in temperature, 5, 1, 2 in 12.5 μm opacity, and 5, 2, 1 in silicate absorption. The patchy distribution of absorption, with no clear correspondence with continuum features, confirms

our suggestion that the silicate absorption is very localized, not just at the compact sources, but throughout the cloud.

4.3.3. *DR 21*

Figure 12 shows the silicate absorption in DR 21 compared with the 20.6 μm flux. The absorption structure is relatively smooth toward DR 21 N. At the southwestern source, on the other hand, the distribution is once again clumpy and not well correlated with the 20.6 μm structure. As in the Mon R2 ring, some 20.6 μm features roughly correspond to absorption peaks (e.g., [−8, −14] or [−7, −7]), while others do not (e.g., [−16.5, −14] or [−9, +3]). When compared to the color temperature and 12.5 μm opacity maps, once again there is no clear correlation of absorption features with temperature or opacity features (although the signal-to-noise ratio in DR 21 is not as high as in the other star-forming regions). The high-opacity ridge in DR 21 S shows silicate absorption, as in the ring of Mon R2. The hot dust at DR 21 N has an absorption factor of $f \sim 4$–5, whereas the hot dust near [RGG89] A has a factor of only $f \sim 2.5$.

5. CONCLUSIONS

1. Deep silicate absorption is present in each star-forming region. In W51 IRS 2 and Mon R2, the absorption is highly localized, as it was in NGC 6334I (Kraemer et al. 1999a). We suggest that the silicate absorption toward the compact sources is due to circumstellar material such as disks or shells.

2. For sources with complete spectral information, simple dust models were fitted to the spectral energy distributions (SEDs). These constrained the optical depth $\tau_{9.7}$ to approximately 2–5, which is consistent with more complex dust models fitted to compact H II regions. For sources without complete spectral information, a simple test was devised based on the shape of the SED for $\lambda > 10$ μm. Based on a Kolmogorov-Smirnov test, the incomplete sources are significantly more likely to have silicate absorption than not.

3. Maps of the "absorption factor" f, roughly the ratio of the continuum to the depth of the silicate absorption feature, were made for W51 IRS 2, Mon R2, and DR 21. No consistent correlation was found between f and either dust color temperature or 12.5 μm opacity. The grains producing the silicate absorption feature are therefore not the same as those responsible for the 12.5 μm opacity.

4. In W51 IRS 2, the two previously known mid-IR sources have been resolved into at least five subsources, and at least six new mid-IR compact sources in and around the extended envelope of mid-IR emission have been detected. The gas density in the ring at Mon R2 supports the blister scenario for the IRS 1 H II region. We suggest that the infrared source in the southwest of DR 21 is not self-luminous, but instead is heated by the three nearby radio continuum sources, particularly radio source [RGG89] A.

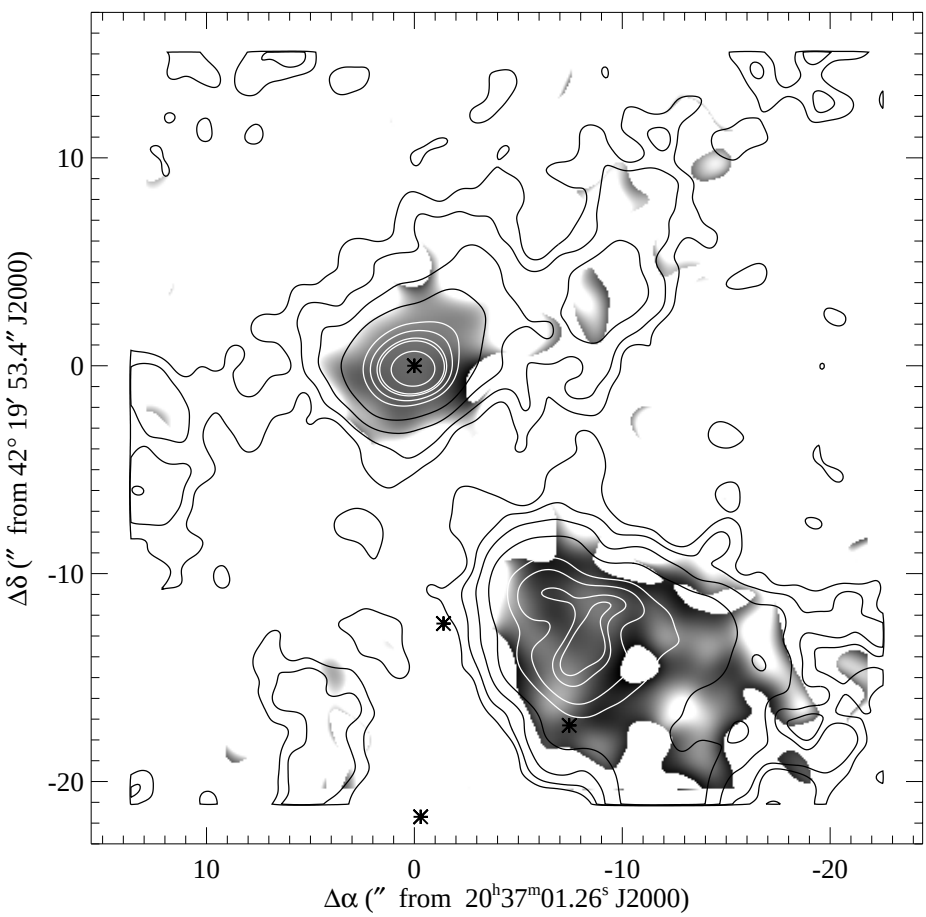

FIG. 12.—Silicate absorption distribution for DR 21 (*gray scale*; $2 < f < 17$). The 20.6 μm continuum emission is superposed (contours, smoothed to 2″). Radio continuum sources [RGG89] A, B, C, and D are marked with asterisks.

Infrared counterparts are newly reported for two radio-continuum sources in S140, and two new mid-IR sources have been tentatively detected at 20.6 μm.

We would like to thank the anonymous referee, whose careful reading added to the clarity of this paper. We would like to thank the telescope operators of the IRTF for their assistance during the observations. K. E. K. would like to thank the National Research Council for support via a Research Associateship through the Air Force Office of Scientific Research. This work was supported in part by start-up funds to L. K. D. from Boston University. This research has made use of NASA's Astrophysics Data System Abstract Service, SIMBAD, the on-line Dictionary of Nomenclature of Celestial Objects of the CDS, and IRAF. IRAF is written and supported by the IRAF programming group at the National Optical Astronomy Observatories (NOAO) in Tucson, Arizona. NOAO is operated by the Association of Universities for Research in Astronomy (AURA), Inc. under cooperative agreement with the National Science Foundation. The HEARSARC Web-based coordinate converter was used the precess the B1950 coordinates from the literature (§ 2) to J2000.

REFERENCES

Adams, F. C. 1993, in ASP Conf. Ser. 35, Massive Stars: Their Lives in the Interstellar Medium, ed. J. P. Cassinelli & E. B. Churchwell (San Francisco: ASP), 56
Arens, J. F., Lamb, G. M., Peck, M. C., Moseley, H., Hoffmann, W. F., Tresch-Fienberg, R., & Fazio, G. G. 1984, ApJ, 279, 685
Aspin, C., & Walther, D. M. 1990, A&A, 235, 387
Becklin, E. E., Beckwith, S., Gatley, I., Matthews, K., Neugebauer, G., Sarazin, C., & Werner, M. W. 1976, ApJ, 207, 770
Beichman, C. A., Becklin, E. E., & Wynn-Williams, C. G. 1979, ApJ, 232, L47
Blair, G. N., Evans, N. J., II, vanden Bout, P. A., & Peters, W. L., III 1978, ApJ, 219, 896
Campbell, M. F., Hoffmann, W. F., Thronson, H. A., Jr., Niles, D., Nawfel, R., & Hawrylycz, M. 1982, ApJ, 261, 550
Cohen, M., Witteborn, F. C., Walker, R. G., Bregman, J. D., & Wooden, D. H. 1995, A&A, 110, 275
Crampton, D., & Fischer, W. A. 1974, Publ. Dom. Astrophys. Obs. Victoria, 14, 12
Davis, C. J., & Smith, M. D. 1996, A&A, 310, 961
Dickel, H. R., Goss, W. M., Rots, A. H., & Blount, H. M. 1986, A&A, 162, 221
Downes, D., Winnberg, A., Goss, W. M., & Johansson, L. E. B. 1975, A&A, 44, 243
Draine, B. T., & Bertoldi, F. 1996, ApJ, 469, 269
Evans, N. J., II, Mundy, L. G., Kutner, M. L., & Depoy, D. L. 1989, ApJ, 346, 212
Faison, M., Churchwell, E., Hofner, P., Hackwell, J., Lynch, D. K., & Russell, R. W. 1998, ApJ, 500, 280
Fisher, J., Sanders, D. B., Simon, M., & Solomon, P. M. 1985, ApJ, 293, 508
Forrest, W. J., Gillett, F. C., & Stein, W. A. 1975, ApJ, 195, 423
Garden, R., & Carlstrom, J. E. 1992, ApJ, 392, 602
Garden, R., Geballe, T. R., Gatley, I., & Nadeau, D. 1986, MNRAS, 220, 203
Garden, R., Russell, A. P. G., & Burton, M. G. 1990, ApJ, 354, 232
Gaume, R. A., Johnston, K. J., & Wilson, T. L. 1993, ApJ, 417, 645
Gaume, R. A., & Mutel, R. 1987, ApJS, 65, 193
Genzel, R., Becklin, E. E., Wynn-Williams, C. G., Moran, J. M., Reid, M. J., & Jaffe, D. T. 1982, ApJ, 255, 527
Genzel, R., & Downes, D. 1979, A&A, 72, 234
Gezari, D. Y., Backman, D. E., & Werner, M. W. 1998, ApJ, 509, 283
Gezari, D. Y., Schmitz, M., Pitts, P. S., & Mead, J. M. 1993, Catalog of Infrared Observations (3d ed.; NASA RP-1294)
Gezari, D. Y., Shu, P., Lamb, G., Tresch-Fienberg, R., Fazio, G. G., Hoffmann, W. F., Gatley, I., & McCreight, C. 1985, ApJ, 299, 1007
Goldader, J. D., & Wynn-Williams, C. G. 1994, ApJ, 433, 164
Hackwell, J. A., Grasdalen, G. L., & Gehrz, R. D. 1982, ApJ, 252, 250
Hanner, M. S., Brooke, T. Y., & Tokunaga, A. T. 1995, ApJ, 438, 250
Harris, S. 1973, MNRAS, 162, 5p
Harvey, P. M., Joy, M., Lester, D. F., & Wilking, B. A. 1986, ApJ, 300, 737
Hayashi, M., Hasegawa, T., Omodaka, T., Hayashi, S. S., & Miyawaki, R. 1987, ApJ, 312, 327
Hayashi, M., & Murata, Y. 1992, PASJ, 377, 391
Hildebrand, R. D. 1983, QJRAS, 24, 267
Hoffmann, W. F., Fazio, G. G., Shivanandan, K., Hora, J. L., & Deutsch, L. K. 1994, Infrared Phys. Tech., 35, 175
Hoffmann, W. F., Hora, J. L., Fazio, G. G., Deutsch, L. K., & Dayal, A. 1998, in Infrared Astronomical Instrumentation, ed. A. M. Fowler, Proc. SPIE 3354, 647
Howard, E. M., Pipher, J. L., & Forrest, W. J. 1994, ApJ, 425, 707
Johnston, K. J., Sloanaker, R. M., & Bologna, J. M. 1973, ApJ, 182, 67
Jones, B., Merrill, K. M., Stein, W., & Willner, S. P. 1980, ApJ, 242, 141
Kraemer, K. E., Deutsch, L. K., Jackson, J. M., Hora, J. L., Fazio, G. G., Hoffmann, W. F., & Dayal, A. 1999a, ApJ, 516, 817
Kraemer, K. E., Jackson, J. M., Deutsch, L. K., Hora, J. L., Fazio, G. G., Hoffmann, W. F., & Dayal, A. 1999b, BAAS, 194, 68.04
Kraemer, K. E., Price, S. D., Sloan, G. C., & Walker, H. J. 2001, ApJS, submitted
Lane, A. P., Haas, M. R., Hollenbach, D. J., & Erickson, E. F. 1990, ApJ, 361, 132
Massi, M., Felli, M., & Simon, M. 1985, A&A, 152, 387
Mathis, J. S. 1971, ApJ, 167, 261
Mauersberger, R., Henkel, C., & Wilson, T. L. 1987, A&A, 173, 352
Men'shchikov, A. B., & Henning, T. 1997, A&A, 318, 879
Mezger, P. G., & Henderson, A. P. 1967, ApJ, 147, 471
Migenes, V., Johnston, K. J., Pauls, T. A., & Wilson, T. L. 1989, ApJ, 347, 294
Natta, A., & Panagia, N. 1976, A&A, 50, 191
Palagi, F., Cesaroni, R., Comoretto, G., Felli, M., & Natale V. 1993, A&AS, 101, 153
Panagia, N. 1975, A&A, 42, 139
Pipenbrink, A., & Wendker, H. J. 1988, A&A, 191, 313
Plambeck, R. L., & Menten, K. M. 1990, ApJ, 364, 555
Poglitsch, A., Herrmann, F., Genzel, R., Madden, S. C., Nikola, T., Timmermann, R., Geis, N., & Stacey, G. J. 1996, ApJ, 462, L43
Roelfsema, P. R., Goss, W. M., & Geballe, T. R. 1989, A&A, 222, 247
Schneps, M. H., Lane, A. P., Downes, D., Moran, J. M., Genzel, R., & Reid, M. J. 1981, ApJ, 249, 124
Simon, M., Felli, M., Cassar, L., Fischer, J., & Massi, M. 1983, ApJ, 266, 623
Slysh, V. I., Kalenskii, S. V., Val'tts, I. E., Golubev, V. V., & Mead, K. 1999, ApJS, 123, 515
Smith, N., et al. 2000, ApJ, 540, 316
Sonnhalter, C., Preibisch, T., & Yorke, H. W. 1995, A&A, 299, 545
Stacey, G. J., Jaffe, D. T., Geis, N., Genzel, R., Harris, A. I., Poglitsch, A., Stutzki, J., & Townes, C. H. 1993, ApJ, 404, 219
Sternberg, A., & Dalgarno, A. 1989, ApJ, 338, 197
Tielens, A. G. G. M., & Hollenbach, D. 1985, ApJ, 291, 722
Tokunaga, A. 1986, IRTF Photometry Manual (Honolulu: Univ. Hawaii Instit. Astron.)
Whittet, D. C. B. 1992, Dust in the Galactic Environment (Bristol: IPP)
Wilson, T. L., & Mauersberger, R. 1990, A&A, 239, 305
Wood, D., & Churchwell, E. 1989, ApJS, 69, 31
Wolf, G. A., Lada, C. J., & Bally, J. 1990, AJ, 100, 1892
Wynn-Williams, C. G., Becklin, E. E., & Neugebauer, G. 1974, ApJ, 187, 473
Yao, Y., Hirata, N., Ishii, M., Nagata, T., Ogawa, Y., Sato, S., Watanabe, M., & Yamashita, T. 1997, ApJ, 490, 281
Yao, Y., Ishii, M., Nagata, T., Ogawa, Y., Sato, S., Watanabe, M., & Yamashita, T. 1998, ApJ, 500, 320
Zhang, Q., & Ho, P. T. P. 1995, ApJ, 450, L63
Zhang, Q., Ho, P. T. P., & Ohashi, N. 1998, ApJ, 494, 636